Conf-910728--10-Rev.1

UCRL-JC--106023-Rev.1

DE91 010463

Estimates of Permeability and Relative Permeability for Sandstone Using Image Analysis of Cross Sections

S. C. Blair
J. G. Berryman

THIS PAPER WAS PREPARED FOR SUBMITTAL TO
Proceedings of the
32nd US Rock Mechanics Symposium
Norman, Oklahoma
July 10-12, 1991.

March 1991

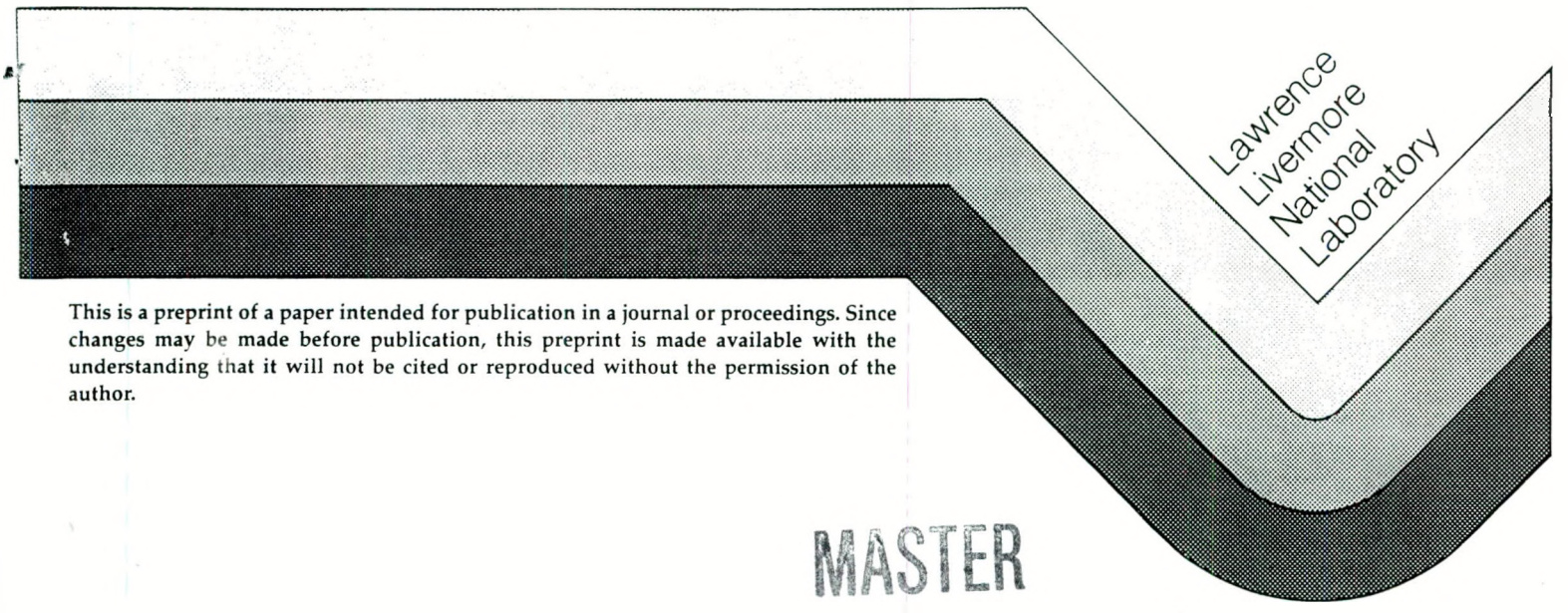

Estimates of permeability and relative permeability for sandstone using image analysis of cross sections

S. C. Blair
University of California
Lawrence Livermore National Laboratory
P. O. Box 808
Livermore, CA 94550

J. G. Berryman
University of California
Lawrence Livermore National Laboratory
P. O. Box 808
Livermore, CA 94550

ABSTRACT: Important geometrical features of the pore space of rocks can be determined from digitized images of rock cross sections. One approach computes statistical correlation functions using modern image processing techniques. These correlation functions contain information about porosity, specific surface area, tortuosity, formation factor, and elastic constants, as well as the fluid and relative permeabilities. The physical basis of this approach is discussed and examples of the results for Berea sandstone are presented. The analysis shows that Kozeny-Carman relations and Archie's empirical laws must be modified to account for finite percolation thresholds and avoid unphysical behavior in the calculated relative permeabilities.

1 INTRODUCTION

Most rocks are porous to some degree. Two properties of practical interest are the fluid permeability and the electrical conductivity of rocks containing conducting fluids. Brace (1977) and Walsh and Brace (1984) have shown that a type of Kozeny-Carman relation may be used to relate the fluid permeability to the electrical formation factor. Walsh and Brace (1984) rederived the Kozeny-Carman relation and wrote it in terms of the porosity, specific surface area, and formation factor. Berryman and Blair (1986) proposed using image processing methods as a means of estimating the parameters in this Kozeny-Carman relation and tested this approach on porous glass and various sandstones. The results from image processing were similar to those of Brace (1977) in that the predicted and measured permeabilities generally agreed well within a factor of 2.

In this paper, we extend our analysis to include traditional relative permeability (k_r) and estimates of k_r for Berea sandstone. In this analysis, interactions between the two fluid phases are neglected and each fluid phase is treated as a single phase flowing through a porous matrix composed of the solid phase and the other fluid phase.

2 SPECIFIC SURFACE AREA FOR TWO FLUIDS

A simple sum rule can be derived relating the various surface areas when two fluids are present. Figure 1(a) shows the simplest geometrical arrangement when one of the two fluids completely wets the surface area of the rock. Then, the nonwetting fluid introduces a fluid/fluid interface. From Fig. 1(b) it is clear that the specific surface area for the

wetted pore space (s_W) is equal to the combined specific surface area for the total pore space (s_T) and the specific surface area for the fluid/fluid interface (s_I), while the specific surface area for the nonwetted pore space (s_{NW}) is equal to s_I. Thus, the sum of the two gives the general result

$$s_W + s_{NW} = s_T + 2s_I. \tag{1}$$

However, if the two fluids occupy separate pore spaces, we have $s_W + s_{NW} = s_T$ because there is no fluid/fluid interface. Furthermore, Eq. (1) is still valid, because the surface area of one fluid will be of the form $s_W = \omega s_T + s_I$ while the other will be of the form $s_{NW} = (1 - \omega)s_T + s_I$, where ω is the wetting fraction and $0 \le \omega \le 1$. Summing these two expressions again gives Eq. (1). Note that Eq. (1) may be used to compute the fluid/fluid interface area per unit, since it implies that

$$s_I = \frac{1}{2}(s_W + s_{NW} - s_T). \tag{2}$$

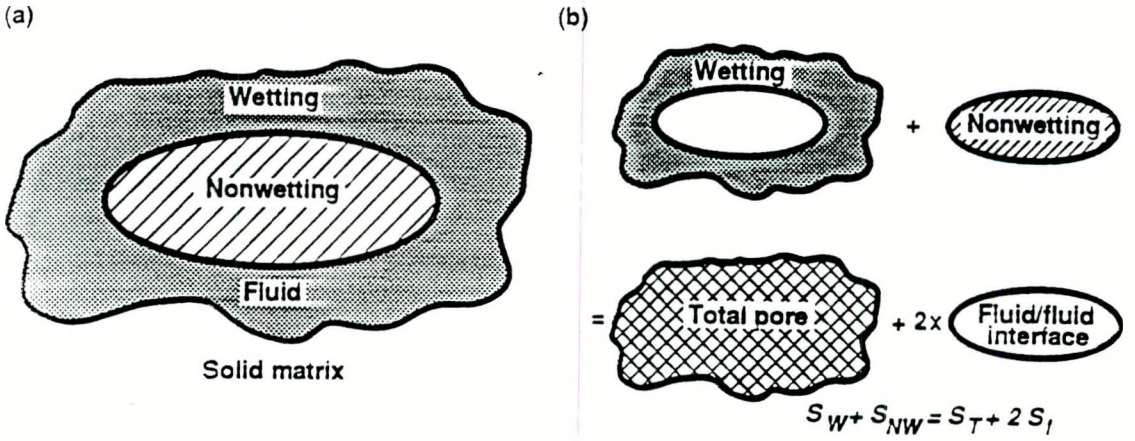

Fig. 1. (a) Geometrical arrangement of wetting and nonwetting fluids in a typical pore. (b) Illustration of the sum rule presented in Eq. (1).

3 KOZENY-CARMAN RELATIONS

The Kozeny-Carman relation for single-phase flow derived by Walsh and Brace (1984) and used extensively by Berryman and Blair (1986; 1987) is given by

$$k = \frac{\phi^2}{2s^2F} = \frac{\phi^3}{2s^2\tau^2}, \tag{3}$$

where ϕ is the porosity, s is the specific surface area, F is the electrical formation factor, τ is the electrical tortuosity, and the relationship $\tau^2 = \phi F$ is applied to the second part of Eq. (3). When two fluid phases are present in the pore space, we distinguish between two types of wetting behavior. Normal wettability refers to the situation where one phase tends to wet the pore surface area, but the second phase tends not to wet it as long as the other phase is present in sufficient quantity. Mixed wettability refers to the situation where both phases tend to wet distinct parts of the pore space regardless of their relative concentrations.

Equation (3) shows that the electrical tortuosity has an important effect on the two-phase flow. To a first approximation, we assume that when both fluids percolate (i.e., form a continuous connected phase) throughout the porous sample, the effective tortuosity for each fluid phase is the same as that for the porous solid. This can be expressed by

$$\phi F = \tau^2 = \tau_W^2 = \tau_{NW}^2. \tag{4}$$

Equation (4) is clearly an approximation that must be modified when the saturation level of either phase approaches the percolation threshold (c). In this case, we can introduce into Eq. (4) additional factors of

$$(\phi_W - \phi_W^c)^\alpha, \qquad (\phi_{NW} - \phi_{NW}^c)^\beta \tag{5}$$

where the critical volume fractions or percolation thresholds for the wetting and non-wetting phases are given respectively by ϕ_W^c and ϕ_{NW}^c and the exponents α and β will be determined through experiment (Bernabé et al., 1982). Typical values of these exponents were shown to be $\alpha \cong \beta \cong 2$ for water saturations down to about 0.15–0.20 (Archie, 1942; Sen et al., 1981). Equation (4) is then modified to

$$\tau^2 = \tau_W^2 [\phi W - \phi_W^c)/\phi]^\alpha = \tau_{NW}^2 [(\phi NW - \phi_{NW}^c)/\phi]^\beta. \tag{6}$$

In general, we expect the percolation thresholds to be small fractions approximately equal to 0.02. With these volume fractions, we can also associate critical saturations levels $\theta_W^c = \phi_W^c/\phi$ and $\theta_{NW}^c = 1 - \phi_{NW}^c/\phi$, where θ is the wetting phase saturation.

Applying both the Kozeny-Carman relation in Eq. (3) and the approximation in Eq. (5) to the separate fluid phases, we have

$$k_W = \frac{\phi_W^3}{2 s_W^2 \tau_W^2} \quad \text{and} \quad k_{NW} = \frac{\phi_{NW}^3}{2 s_{NW}^2 \tau_{NW}^2} \tag{7a.b}$$

If the picture in Fig. 1(a) is typical of the fluid arrangement in the pores, we can expect to find that $s_W = s_T + s_I$ and $s_{NW} = s_I$. Then, the relative permeabilities are given by

$$k_{rW} = \frac{k_W}{k} = \frac{\theta^3}{(s_W/s_T)^2} = \frac{\theta^3}{(1 + s_I/s_T)^2} \tag{8}$$

and

$$k_{rNW} = \frac{k_{NW}}{k} = \frac{(1-\theta)^3}{(s_{NW}/s_T)^2} = \frac{(1-\theta)^3}{(s_I/s_T)^2} \tag{9}$$

thereby cancelling the tortuosity out of these expressions.

Again, if Fig. 1(a) is representative of the distribution of nonwetting fluid to wetting fluid, then to a reasonable approximation we should expect that

$$s_I \cong (1-\theta)\, s_T \tag{10}$$

So, continuing to neglect the effects of the changing tortuosity close to a percolation threshold, we should find that

$$k_{rW} \cong \frac{\theta^3}{[1+(1-\theta)^2]} \quad \text{and} \quad k_{rNW} \cong (1-\theta). \tag{11a,b}$$

The results in Eq. (11a,b) show that we should expect a strong asymmetry between the relative permeabilities for the wetting and the nonwetting phases. These first approximations of the relative permeabilities show that the relative permeability for the wetting phase is a strongly nonlinear function of the wetting phase saturation. Physically, this makes sense because the wetting phase is trapped between the solid and the nonwetting fluid, so the typical open throat for the wetting phase is significantly smaller in the presence of the nonwetting phase. By contrast, the nonwetting phase sees a porous medium that is very similar to that of the solid matrix because the effective pores have just been reduced in size by the coating action of the wetting phase. Until percolation threshold effects become important, the relative permeability for this phase should in fact be proportional to $(1-\theta)$ as shown in Eq. (11b).

If we can measure the various specific surface areas, we can easily determine whether the behavior of normal wettability or that of mixed wettability applies. For normal wettability we find that $s_{NW} = s_I$, while for mixed wettability we find that $s_{NW} > s_I$. The interface area itself may still be computed from Eq. (2). Recalling that for mixed wettability $s_W = \omega s_T + s_I$ and $s_{NW} = (1-\omega)s_T + s_I$ where ω is the relative wetting fractions, we must modify the formulas in Eqs. (8) and (9), so that the relative permeabilities are given by

$$k_{rW} = \frac{k_W}{k} = \frac{\theta^3}{(s_W/s_T)^2} = \frac{\theta^3}{(\omega + s_I/s_T)^2} \tag{12}$$

and

$$k_{rNW} = \frac{k_{NW}}{k} = \frac{(1-\theta)^3}{(s_{NW}/s_T)^2} = \frac{(1-\theta)^3}{(1-\omega+s_I/s_T)^2}. \tag{13}$$

4 SAMPLE PREPARATION AND IMAGE PROCESSING METHODOLOGY

We used a sample preparation and image processing methodology to produce and analyze images of Berea sandstone in which the pore space was segregated into regions occupied by wetting and nonwetting phases. First, a low-melting-point bismuth metal alloy was imbibed into a dry evacuated core sample of Berea sandstone at a temperature of approximately 100°C. After imbibition, we cooled the sample to room temperature, solidifying the metal alloy. Then, we cut the core sample into slabs perpendicular to its axis and chose a slab from the lower section of the sample for our analysis. We vacuum impregnated the slab with epoxy and prepared a standard petrographic thin section. Using a scanning electron microscope (SEM) in back-scatter mode, we examined the thin section. In this mode, the metal (nonwetting) phase appeared bright, while the epoxy (wetting) phase appeared dark and the mineral (grains) phase had intermediate brightness. We then digitized hard copy images of the pore structure and produced images of the total

porosity and segments of the pore space occupied by the wetting and nonwetting phases using standard thresholding techniques.

5 RESULTS

We determined total porosity and the amount of pore space occupied by the nonwetting and wetting phases from four images with magnifications of 54 and 100x. Figure 2(a) shows a representative image and Fig. 2(b) shows the segregated pore space. These images show that, as expected, the nonwetting phase filled most of the large pores. We simply calculated the fraction of pore space occupied by each phase and the results are presented in Table 1. We determined the value of total porosity to be 0.23, which agrees well with values determined from laboratory measurements. Laboratory data indicate that the bulk saturation of the rock with the nonwetting phase was approximately 0.57. However, saturation varied widely over the length of the core and our value of 0.77 at the location of the slab provides precise data on the fine-scale distribution of the nonwetting phase.

We calculated two-point autocorrelation functions (S_2) for images of the total pore space and of the pore space occupied by each phase, following the technique developed by Berryman (1985), and Berryman and Blair (1986). Figure 2(c) shows that the correlation function for the nonwetting, imbibed phase closely resembles the correlation function for the total pore space. This was typical for the images we analyzed and is consistent with our previous observation that the nonwetting phase sees a porous medium that is similar to the solid matrix. Mean grain size can also be estimated from the correlation function, and our results indicate a value of 80 microns.

We also analyzed four images with magnifications in the range 220 to 1100x. We used images at this magnification to estimate the specific surface areas, following the work of Debye, Anderson, and Brumberger (1957), who showed that the derivative of the two-point correlation function near the origin is proportional to the specific surface area, and Berryman and Blair (1987) who related the resolution appropriate for measure s_T to the correlation length computed for the material. Figure 3(a) shows a representative image and Fig. 3(b) shows the segregated pore space. We again calculated the two-point autocorrelation functions for images of the total pore space and of the pore space occupied by each phase. Figure 3(c) shows that, at this scale, the correlation function for the total pore space is not dominated by either pore phase.

To estimate the specific surface area s_T for the total pore space, we fit a line to the first few points of the function S_2 for each image of the total pore space. The slopes of these lines were then averaged to produce a value of S_2 for the total pore space of the cross section; this value is given in Table 1. We then calculated $s_T = 4S_2(0)$ following Berryman and Blair (1986). We also calculated values of specific surface area for both the wetting and nonwetting phases in a similar fashion (Table 1). The value of 0.1072 for s_T agrees well with the values of 0.1109 and 0.1231, which we previously reported for a different sample of Berea sandstone (Berryman and Blair, 1986). We then used the estimates of specific surface area to calculate specific surface area of the fluid/fluid interface following Eq. (2). We estimated ω to be 0.74 and the ratio of the fluid/fluid interface surface area to the total surface area was found to be 0.087, both of which are consistent with the image observations. Thus, the wetting phase does, in fact, cover most of the surface area and the wetting and nonwetting phases do not actually have much

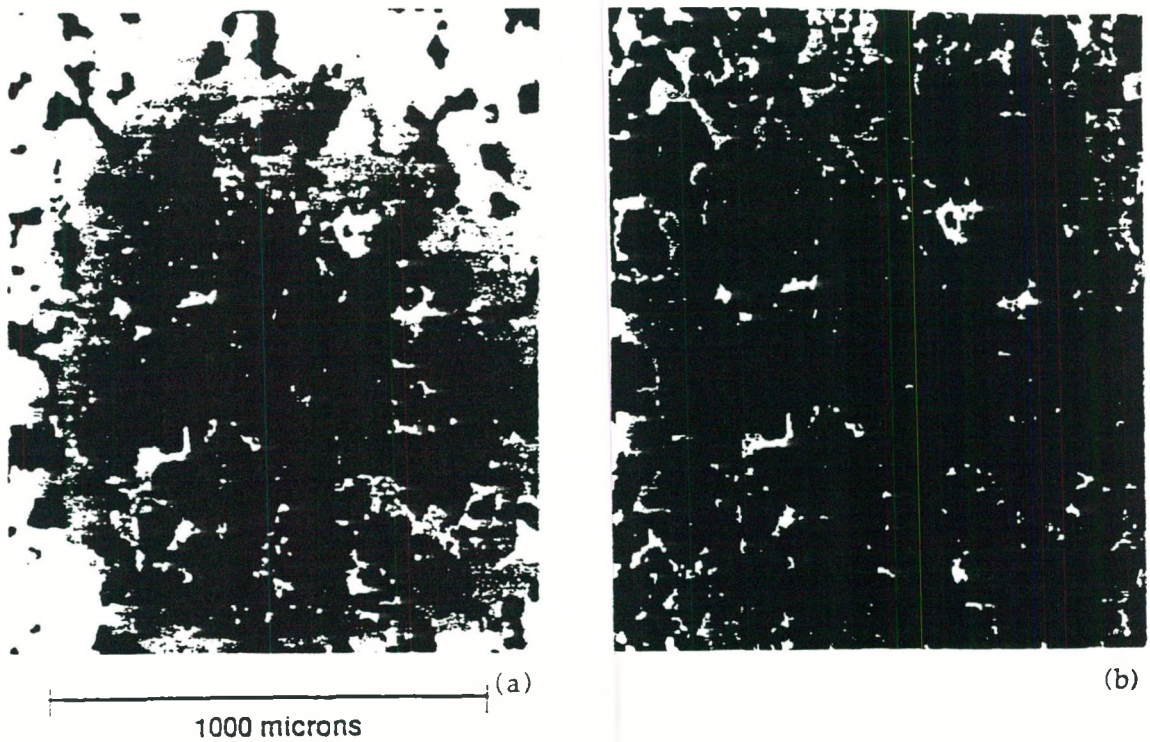

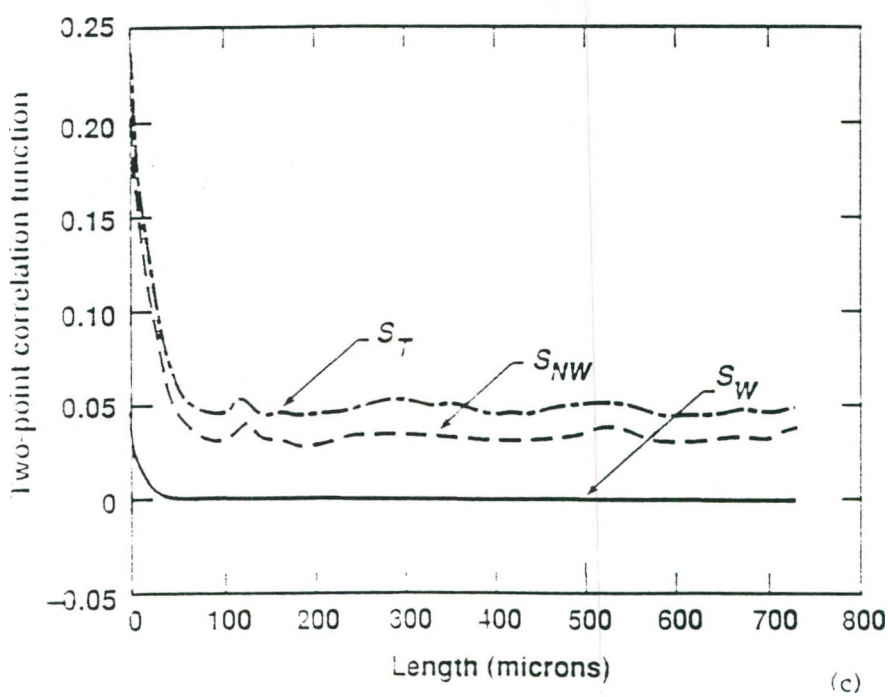

Fig. 2. (a) Image of Berea sandstone at 54x magnitude before segmentation. (b) Image of Berea sandstone after segmentation into solid grains (black), nonwetting (gray) and wetting (white) phases. (c) Two-point correlation functions for Berea sandstone: the total pore space is S_T, the wetted pore space is S_W, and the nonwetted pore space is S_{NW}.

Table 1. Summary of measured parameters for Berea sandstone using image processing techniques.

	Fraction of Total Pore Space	Two-point Spatial Correlation Function (μm)	Specific Surface Area (μm)	Relative Permeability	Effective Hydraulic Radius (μm)
Total Pore Space	1.00	0.0268	0.1072	—	2.10
Wetted Pore Space	0.23	0.0220	0.0881	0.01	4.63
Nonwetted Pore Space	0.77	0.0094	0.0377	2.24	0.58

interfacial contact throughout the sample. These results show that the pore space occupied by the wetting phase has the larger contribution to the total specific surface area.

We estimated permeability for the cross section using the computed values of porosity and specific surface area in conjunction with Eq. (3). We assumed a value of 10.0 for the formation factor and estimated the intrinsic permeability of the rock to be 220 microdarcies (md). This is within a factor of two of the value of 350 md measured in the laboratory for the specimen. We also estimated relative permeability for the wetting and nonwetting phases using Eqs. (12) and (13). The calculated values are given in Table 1. Although the results for the wetting phase were quantitatively sensible ($k_{rW} \cong 0.01$), the results for the nonwetting phase were not. In fact, the computed relative permeability for the nonwetting phase was found to be greater than unity.

To improve our estimates of relative permeability, we incorporated Eq. (6) into Eqs. (7a,b). Therefore, assuming $\alpha = \beta = 2$, the expressions in Eqs. (12) and (13) can be written as

$$k_{rW} = \frac{\theta^3(\theta - \theta^c_{W})^2}{(s_W/s_T)^2} \quad \text{and} \quad k_{rNW} = \frac{(1-\theta)^3\,(\theta^c_{NW} - \theta)^2}{(s_{NW}/s_T)^2} \tag{14a,b}$$

where the relative permeabilities are no longer expressed as only functions of the saturation and surface areas, but are now also dependent on the percolation thresholds. We do not have an independent measure of the value of the percolation threshold for the nonwetting phase, but it is interesting to note that we can use Eq. (14b) together with the assumption that $k_{rNW} \leq 1$, to obtain an estimate of the value of the percolation threshold. This computation shows that $(1 - \theta^c_{NW})\phi \geq 0.05$ and that $\theta^c_{NW} < 0.75$. These numbers are completely consistent with the fact that the measured nonwetting saturation is $1 - \theta \cong 0.77 \geq 0.25 \cong 1 - \theta^c_{NW}$.

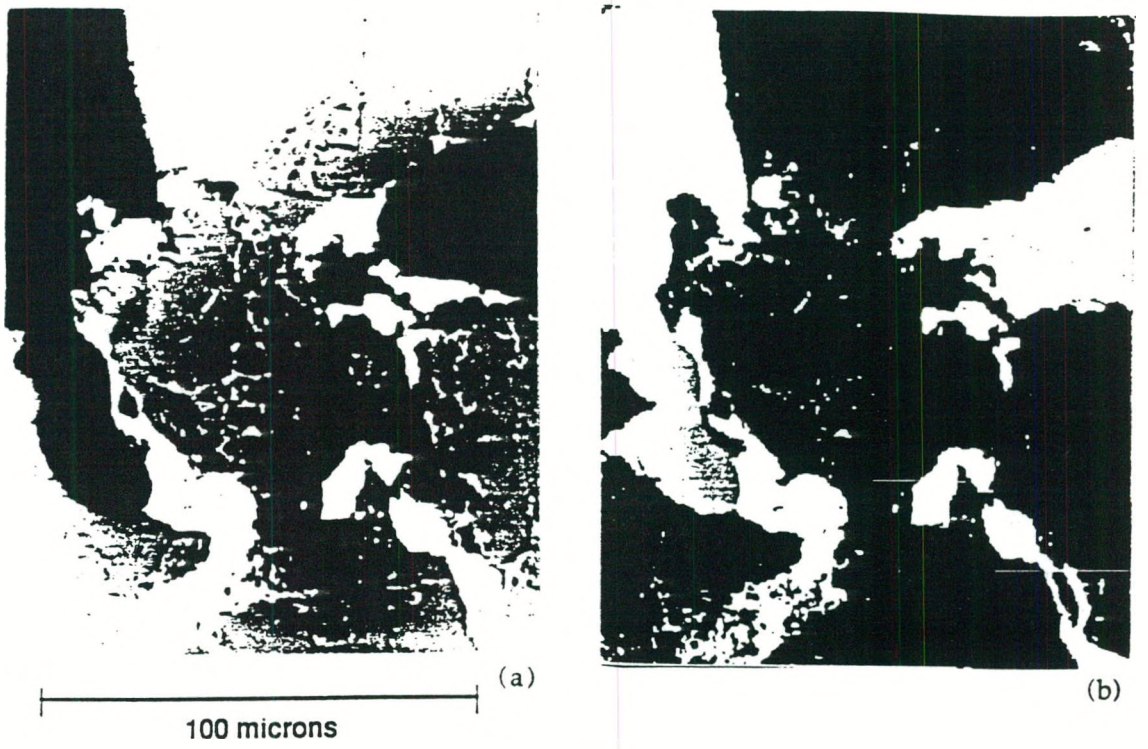

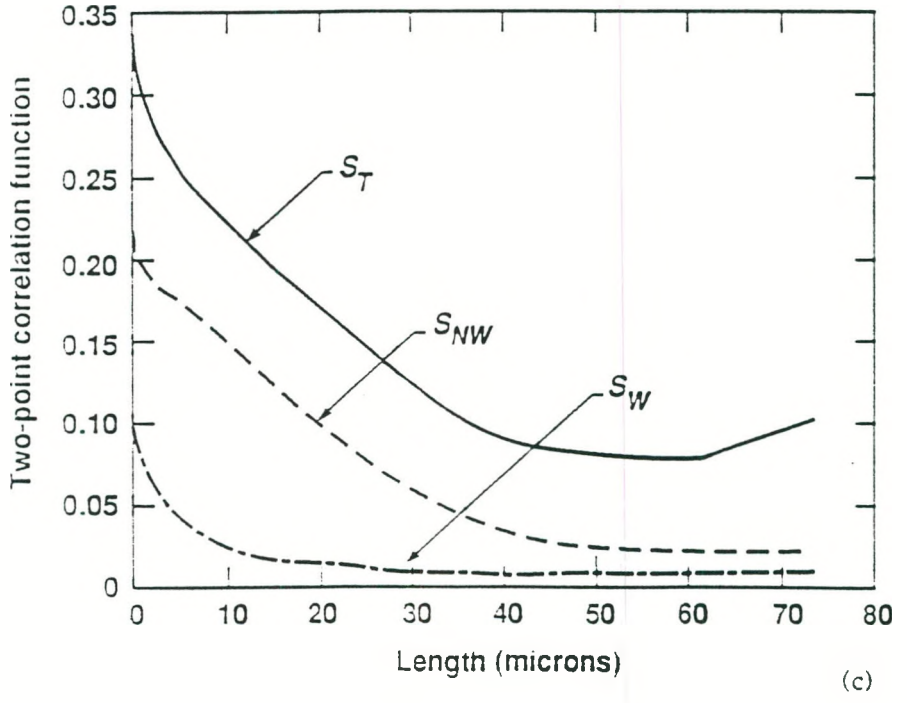

Fig. 3. (a) Image of Berea sandstone at 540x magnitude before segmentation. (b) Image of Berea sandstone after segmentation into solid grains (black), nonwetting (gray) and wetting (white) phases. (c) Two-point correlation functions for Berea sandstone: the total pore space is S_T, the wetted pore space is S_W, and the nonwetted pore space is S_{NW}.

Another nonrigorous relation we can use to gain information is the approximate relation $\theta_W^c \cong 1 - \theta_{NW}^c$ between the percolation thresholds for the wetting and the nonwetting phases. Thus, we find that $\theta_W^c \cong 0.25$ with some experimental error. The measured value of the wetting saturation was 0.23, so the wetting phase was imbibed at close to its percolation threshold.

We also used the specific surface area for each phase with the fractional pore volume of each phase to compute the effective hydraulic radius equal to ϕ/s, for the total and segregated pore space. These values (shown in Table 1) indicate that the effective hydraulic radius of the pore space occupied by the nonwetting phase is larger than that of the total pore space. The results show qualitatively that the wetting phase dominates the specific surface area, while the nonwetting phase dominates the permeability due to its higher partial saturation. This also indicates that for the imaged cross section, the wetting phase is filling the dead-end pores, and that much of the specific surface area is contained in those dead-end pores.

6 DISCUSSION

Our analysis has stressed two-phase flow through porous media, but it should be clear that generalization to multiphase flow is possible. For example, Oak, Baker, and Thomas (1990) summarized the current understanding of relative permeability for three-phase flow. The results given in Eq. (1) for the relationship among the surface areas are also easily generalized to

$$s_{water} + s_{gas} + s_{oil} = s_{pore} + 2s_{w/g} + 2s_{w/o} + 2s_{g/o} \tag{15}$$

The rigorous result for two-phase flow in Eq. (1) has proven to be a very valuable tool for checking the consistency of computed surface areas, and it is expected that Eq. (15) will prove to be similarly useful for three-phase flow analysis.

One of the unexpected results of the analysis presented here was the clear demonstration that Kozeny-Carman relations and Archie's empirical laws must be modified to account for a finite percolation threshold. A simplified theory that ignores the percolation thresholds leads to unphysical values (> 1) for the relative permeability of the nonwetting phase. Including the percolation thresholds in the calculations leads to a set of physically reasonable numbers for the various permeabilities, and for the threshold values themselves. This approach cannot be used to find accurate estimates of the percolation threshold values since the exponents α and β must be determined simultaneously, but with assumed values for the exponents, a consistent picture of the physical parameters can be obtained.

ACKNOWLEDGMENTS

Deepak Agrawal (U.C. Berkeley) provided the sample for analysis and N. G. W. Cook (U.C. Berkeley) contributed several useful suggestions. This work was performed under the auspices of the U.S. Department of Energy by the Lawrence Livermore National Laboratory under contract No. W-7405-ENG-48 and supported specifically by the DOE Office of Basic Energy Sciences, Division of Engineering and Geosciences.

REFERENCES

Archie, G.E. 1942. The electrical resistivity log as an aid in determining some reservoir characteristics. *Trans. AIME* 146:54–62.

Bernabé, Y., W.F. Brace & B. Evans 1982. Permeability, porosity, and pore geometry of hot-pressed calcite. *Mech. Mat.* 1:173–183.

Berryman, J.G. 1985. Measurement of spatial correlation functions using image processing techniques. *J. Appl. Phys.* 57:2374–2384.

Berryman, J.G. & S.C. Blair 1986. Use of digital image analysis to estimate fluid permeability of porous materials: Application of two-point correlation functions. *J. Appl. Phys.* 60:1930–1938.

Berryman, J.G. & S.C. Blair 1987. Kozeny-Carman relations and image processing methods for estimating Darcy's constant. *J. Appl. Phys.* 62:2221–2228.

Brace, W.F. 1977. Permeability from resistivity and pore shape. *J. Geophys. Res.* 82:3343–3349.

Debye, P., H.R. Anderson & H. Brumberger 1957. Scattering by an inhomogeneous solid. II. The correlation function and its application. *J. Appl. Phys.* 28:679–683.

Oak, M.J., L.E. Baker & D.C. Thomas 1990. Three-phase relative permeability of Berea sandstone. *J. Petroleum Techn.* 42:1054–1061.

Sen, P.N., C. Scala & M.H. Cohen 1981. A self-similar model for sedimentary rocks with application to the dielectric constant of fused glass beads. *Geophysics* 46:781–795.

Walsh, J.B. & W.F. Brace 1984. The effect of pressure on porosity and the transport properties of rock. *J. Geophys. Res.* 89:9425–9431.

Technical Information Department · Lawrence Livermore Laboratory
University of California · Livermore, California 94550